Assessing the impact of COVID-19-induced lockdown on land surface temperatures in heterogeneous cities

Simbarashe Jombo[1]*, Mohamed A. M. Abd Elbasit[1], Colbert M. Jackson[2], Samuel A. Adelabu[2]
[1]Department of Physical and Earth Sciences, Sol Plaatje University, Kimberley 8300, South Africa, email: simbarashejombo@gmail.com
[2]Department of Geography, Faculty of Natural and Agricultural Sciences, University of the Free State, Bloemfontein, South Africa

DOI: https://dx.doi.org/10.4314/sajg.v14i1.7

Abstract

Urbanisation has brought about significant changes in the land use/land cover (LULC) and land surface temperatures (LSTs) of cities. The impact of the COVID-19 lockdown on LSTs in Polokwane and Johannesburg, South Africa, was analysed over the years 2020 to 2022, using Landsat 8 and 9 images. The relevant LSTs were retrieved by applying the temperature/emissivity separation algorithm. The normalized difference built-up index (NDBI) and the normalized difference vegetation index (NDVI) threshold techniques were used to evaluate the LSTs for the two cities in terms of five LULC classes: bare land, built-up area, road, vegetation, and waterbody. The LST patterns were estimated per LULC class and the Pearson's correlation analysis was performed to examine the relationship between NDVI, NDBI, and LST. The findings revealed that throughout the lockdown period (i.e., from January 2020 to March 2021, there was a decrease in LST values across all LULC categories − by 1°C for vegetation and 2°C for the bare land, built-up, road and waterbody classes. The LST values showed an increase from 2021 (during lockdown) to 2022 (post-lockdown), thereby demonstrating in particular their association with the bareland class, where the most notable increases of 1.9°C and 0.6°C were observed in Polokwane and Johannesburg, respectively. There were strong negative correlations between the NDVI and LST (i.e., -0.62, -0.58, and -0.71 for Polokwane and -0.69, -0.69, and -0.73 for Johannesburg) in 2020, 2021, and 2022, respectively. Strong positive correlations between NDBI and LST (i.e., 0.81, 0.79, and 0.85, and 0.70, 0.59, and 0.77) were recorded in Polokwane and Johannesburg respectively for the same period. The decline in LSTs was due to the cessation of industrial activities, transportation, and other human activities, resulting in improved air quality that in turn reduced the effects of the respective urban heat islands (UHIs). The findings offer valuable information that is vital for decision-making procedures that are in line with the aims of SDG 11 which are to improve the sustainability of cities.

Keywords: *COVID-19 lockdown, Land Surface Temperature (LST), Urban Heat Island (UHI), Land use and Land Cover (LULC), Landsat OLI, Normalized Difference Vegetation Index (NDVI), Normalized Difference Built-up Index (NDBI)*

1. Introduction

Over the next three decades, urban heat island (UHI) events are projected to affect more than 70% of urban areas worldwide (United Nations, 2022). According to the forecasts by the Intergovernmental Panel on Climate Change (IPCC), carbon dioxide (CO_2) levels are projected to increase fourfold from their pre-industrial levels. At the same time, the average global land surface temperature (LST) will rise by 1.4°C to 5.8°C by the year 2100 (Pörtner *et al*., 2022). This significant increase highlights the urgent need for effective climate adaptation strategies. The variable, LST is being increasingly used to measure surface UHI and assess climate change in cities/towns (Amani-Beni *et al*., 2019; Onishi *et al*., 2010). LST refers to the temperature experienced at the interface between the land surface and the atmosphere where turbulent heat fluxes and longwave radiation exchanges occur (Mustafa *et al*., 2020). These factors contribute to the intensification of urban heat islands (UHIs), which are characterised by elevated temperatures in urban areas compared to their rural surroundings.

Rapid urbanisation, industrialisation, and overpopulation, all of which are the leading drivers of environmental degradation and are responsible for significant changes in land use/land cover (LULC), are the leading causes of UHIs (Shikwambana *et al*., 2021; Lu *et al*., 2011). The UHI phenomenon is caused by the removal of the natural land cover (e.g., in the case of wetlands and vegetation) through the construction of roads and buildings, and through anthropogenic heat emissions, such as those generated by cars, air conditioners, and industries (Jallu *et al*., 2022; Onishi *et al*., 2010). Therefore, when roads generally constructed from asphalt, concrete, or other impermeable materials replace vegetation, the natural cooling effects of shading and evapotranspiration are reduced (Onishi *et al*., 2010). Also, dark surfaces, such as roads and rooftops, characteristic of urban areas, absorb solar heat, thereby leading to elevated surface temperatures and a rise in ambient temperatures (Jallu *et al*., 2022; University Corporation for Atmospheric Research, 2011). This phenomenon is compounded by the urban built environment, which enhances heat retention.

Heat islands are generated through high density structures that are quick to absorb heat but slow to release it (Almeida *et al*., 2021). Narrow streets between tall buildings in urban areas tend to confine air between the traffic corridors separating them, thereby causing an additional warming effect (Tarawally *et al*., 2018). Increasing temperatures from UHIs can adversely affect the environment and overall quality of life (Jombo *et al*., 2022). A rise in surface temperatures during the day, reduced cooling at night, and increased air pollution levels related to UHIs may affect human health in the form of heat exhaustion, respiratory-related ailments, heat stroke, and heat-related mortality (Amani-Beni *et al*., 2019; University Corporation for Atmospheric Research, 2011).

As research has indicated, there is a positive correlation between high temperatures and an increase in urban mortality rates, with extreme heat events expected to contribute to a continued

rise in heat-related deaths (Harlan & Ruddell, 2011). With global warming, expectations point to an increase in both the frequency and intensity of severe heat events, thus exacerbating the global risk of morbidity and mortality (Alexander, 2020). Urbanisation dramatically alters the urban microclimate, thereby increasing the consequences of global warming (Jombo *et al*., 2022). Those vulnerable to heat-related illnesses are mostly those working outdoors, young children, older people, and chronically ill humans (University Corporation for Atmospheric Research, 2011). As a result, these groups face increased health risks during extreme heat events, highlighting the urgent need for effective public health interventions.

Characteristically, UHIs raise the energy demand, especially during the summer months, by, amongst others, air conditioning units. This in turn intensifies the generation of electricity from combusting fossil fuels (University Corporation for Atmospheric Research, 2011). Pollutants from fossil fuels worsen air quality issues, particularly when higher temperatures prevail (United States Environmental Protection Agency, 2008). Furthermore, fossil fuels emit greenhouse gases, especially CO_2, thereby contributing to global warming (climate change) (University Corporation for Atmospheric Research, 2011). As land surface temperatures (LSTs) rise, glaciers and ice sheets in the polar regions melt, thereby resulting in increased flooding and rising sea levels (Solanky *et al*., 2018). This melting contributes to global climate instability, affecting ecosystems and human settlements alike.

Monsoon countries, also affected by global warming differently, are severely impacted by unpredictable rainfall—the net effect being a depleted vegetation cover unable to protect the exposed ground surface from erosion (Rajeshwari & Mani, 2014). This loss of vegetation further exacerbates environmental challenges, leading to increased vulnerability to flooding and soil degradation. UHIs compromise the quality of the water in that they are responsible for thermal pollution: −the excess heat from hot pavement and rooftop surfaces is transferred to the stormwater drainage channels, thereby increasing the temperature of the water when it is released into rivers and lakes (United States Environmental Protection Agency, 2008).

The thermal enrichment of waterbodies serves to disrupt various aspects of aquatic life, particularly the metabolic and reproductive processes of organisms (University Corporation for Atmospheric Research, 2011). Temperature changes related to UHIs can also alter the accessibility of food and water, thus affecting the eating and foraging habits of animals (Larsen, 2015; University Corporation for Atmospheric Research, 2011). Furthermore, owing to the heat radiating from UHIs, temperate climates typically experience a prolonged growing season, which changes the breeding cycles of species (Shochat *et al*., 2006). Rapid changes in temperature in aquatic ecosystems resulting from warm stormwater runoff can induce stress in marine life (United States Environmental Protection Agency, 2008). This stress is indicative of broader ecological impacts that arise from urbanisation.

Urbanisation and urban land-use change contribute to escalating global LSTs, declining rates of evaporation and precipitation, the extent of the hydrological area, and the level of land degradation (Patra *et al*., 2018). The LULC changes resulting from urbanisation can modify the energy balance of cities, thereby altering the thermal environment within urban areas leading to UHIs (Hart & Sailor, 2009). As a result, urban regions exhibit elevated air and surface temperatures. Therefore, city planners must consider the heat island effect in their urban designs. Consequently, the search for efficient ways in which to mitigate the effects of the UHI phenomenon has emerged as a critical area in urban ecology and planning research. In most studies, the UHI effect is primarily explored by observing its impacts (Errebai *et al*., 2022; Onishi *et al*., 2010), drivers (Li *et al*., 2020), and mitigation strategies to reduce its effects (Wang *et al*., 2016). Understanding these aspects is crucial, especially considering emerging global challenges that affect public health and urban resilience.

Originating in Central China, in the city of Wuhan, in December 2019, the acute respiratory disease known as COVID-19, was brought on by Coronavirus-2 (SARS-CoV-2). COVID-19 triggered a pandemic that resulted in various negative impacts worldwide (Louw *et al*., 2022). The COVID-19 pandemic has proved to be both the deadliest public health calamity of our time and the most formidable challenge to confront humanity since World War II (Ali *et al*., 2021). The COVID-19 outbreak resulted in a substantial rise in global mortality rates, with 764,474,387 reported cases, and 6,915,286 deaths (World Health Organisation, 2023), and significant economic causalities (e.g., the global GDP contracted by 3.3% in 2020) (International Monetary Fund, 2023; Louw *et al*., 2022). March 11, 2020, marked the proclamation by the World Health Organization (WHO) that the COVID-19 outbreak had reached pandemic proportions. Several measures were implemented to mitigate the hazards posed by the COVID-19 pandemic, with mass quarantines, lockdowns, complete travel bans, and social isolation being the order of the day (Jallu *et al*., 2022). However, these risk-taking initiatives have considerably impacted negatively on socioeconomic growth, political relations, and the environment (Louw *et al*., 2022).

During the COVID-19 pandemic, South Africa underwent several phases of lockdown, including a complete lockdown, known as Level 5, which started on 26 March 2020 and lasted until 30 April 2020 (South African Government, 2023). This unprecedented situation provided a unique context for researchers to examine the effects of reduced human activity on urban environments.Several studies (e.g., Maithani *et al*. (2020), Alqasemi *et al*. (2021), Ali *et al*. (2021), Shikwambana *et al*. (2021), and Jallu *et al*. (2022)) investigated the impact of the COVID-2019 lockdown on surface UHIs. These studies underscore a shift in research methodologies prompted by the unique circumstances of the pandemic.

In the traditional approach to studying UHIs, researchers typically collected *in-situ* air temperature measurements at isolated locations. These measurements would then be applied,

through the process of interpolation, to produce isotherm maps (Solanky *et al*., 2018). Furthermore, the mapping of urban temperatures was initially possible only on a regional scale. However, great strides have since been made to access the state-of-the-art technologies now available. The introduction of thermal sensors in Landsat and Sentinel allows for studies of UHIs to be undertaken continuously (Mishra & Garg, 2023). Owing to the high spatial density of urban environments, thermal remote sensing methods are now frequently applied to retrieve the necessary data around LST values to identify UHIs (Maithani *et al*., 2020).

In our current study, the method of using advanced high resolution data obtained through the National Oceanic and Atmospheric Administration Advanced Very High-Resolution Radiometer (NOAA AVHRR) stands in sharp contrast to the initial methods used as described above (Mishra & Garg, 2023). The introduction of the higher resolution Landsat thematic mapper (TM) and Enhanced Thematic Mapper Plus (ETM+) has made the mapping of urban temperatures at the city level possible (Mishra & Garg, 2023). Since the LST is related to the heat of the urban canopy layer (UCL), which may not be contiguous in urban areas, higher resolution remote sensing data are required for the more accurate detection of UHIs. The algorithms used to retrieve LSTs rely on the inversion of Planck's law and compute brightness temperature (BT) from atmospheric radiances acquired through thermal infrared sensors (TIRS) (Mathew *et al*., 2016). Using ground surface emissivity, the BT is then converted to LST (Maithani *et al*., 2020). Numerous algorithms are used to extract the LST from remote sensing data. Examples include the mono-window algorithm (Qin *et al*., 2001), the single-channel algorithm (Jimenez-Munoz *et al*., 2008; Jiménez-Muñoz & Sobrino, 2003), the temperature-emissivity separation algorithm (Gillespie *et al*., 1998), the multi-angle and multi-channel algorithms (Sobrino *et al*., 1996), the split-window algorithm (Sobrino *et al*., 1996), and the radiative transfer equation (Maithani *et al*., 2020). These algorithms play a critical role in accurately assessing LSTs from remote sensing data.

Recent research has established the correlation between LULC and LST by employing spectral indices, including the normalized difference vegetation index (NDVI) (Chakraborty *et al*., 2021; Guha *et al*., 2018; Guha *et al*., 2017; Jallu *et al*., 2022; Liu & Zhang, 2011; Mishra & Garg, 2023; Solanky *et al*., 2018), the normalized difference built-up index (NDBI) (Guha *et al*., 2018; Guha *et al*., 2017; Jallu *et al*., 2022; Liu & Zhang, 2011; Mishra & Garg, 2023; Zha *et al*., 2003), the normalized difference bareness index (NDBaI) (Guha *et al*., 2017; Mishra & Garg, 2023; Zhao & Chen, 2005), the normalized difference water index (NDWI) (Mishra & Garg, 2023), and the modified normalized difference water index (MNDWI) (Guha *et al*., 2017). The representation of LULC classes using the above-mentioned spectral indices and the interpretation of how they relate to LST contributes to an understanding of the nature and behaviour of UHIs over time. (Chen *et al*., 2006).

NDVI (Jackson *et al*., 1983) is usually applied to quantitatively represent the density of healthy vegetation. On the other hand, NDBI (Zha *et al*., 2003) detects changes in built-up areas. The quantification of the relationship between LULC changes and LSTs in urban areas also helps to explain the contribution of anthropogenic activities to the intensity of the UHI phenomenon (Mishra & Garg, 2023). Furthermore, this understanding is reinforced by previous research which indicates that various mitigatory measures implemented to minimise the spread of COVID-19 have lessened the impact of the UHI phenomenon. Previous research (e.g., Maithani *et al*. (2020), Ali *et al*. (2021), Alqasemi *et al*. (2021), Shikwambana *et al*. (2021), and Jallu *et al*. (2022)) reported that the various mitigatory measures implemented to minimise the spread of COVID-19 had lessened the impact of the UHI phenomenon. However, Chakraborty *et al*. (2021) reported enhanced surface UHIs in the Indo-Gangetic Basin, India, even when human activities were minimal.

Our current study intended to examine how the COVID-19 lockdown affected surface UHIs in the context of different LULC types in Polokwane and Johannesburg − both cities in South Africa using Landsat-8 and 9 OLI/TIRS data but under different climatic conditions. The two cities recorded high COVID-19 infection rates (Rachuene *et al*., 2021). However, Polokwane and Johannesburg differ in that, amongst others, they support populations of different sizes and industrial and human activities of different intensities (Statistics South Africa, 2022).

Polokwane city in Limpopo Province is the largest urban centre in the Great North of South Africa. It is considered the commercial and industrial hub of the region and is also known as the ‘gateway city’ because of its wide assortment of game reserves and natural attractions in the region (Rogerson & Rogerson, 2021). Recently, owing to high rates of immigration from nearby countries such as Zimbabwe, Mozambique, and Malawi, its population numbers have been steadily increasing (Khutso *et al*., 2022).

The City of Johannesburg is South Africa’s chief mining, industrial, and financial metropolis — it is the economic hub of southern Africa and therefore experiences high in-migration rates (Rogerson & Rogerson, 2021). Johannesburg is a local, national, and international travel hub. In the past, researchers such as Alexander (2020); Logan *et al*. (2020); Magli *et al*. (2015) focused on analysing the effect of a single LULC type, mainly the built-up area class, on the UHI phenomenon. This study highlighted the significant role that specific land cover types play in influencing urban temperatures. It is worth noting that an understanding of the effect of LULC type on the UHI phenomenon is important to municipalities and other stakeholders involved in urban planning in their quest to enhance sustainable development (Jombo *et al*., 2022). This understanding can inform data-driven decisions that lead to more effective urban management practices.

The objectives of this current study were (i) to extract LSTs from multitemporal Landsat-8 and 9 OLI and TIRS data and to map the spatial distribution of LSTs before January 2020,

during March 2021, and after April 2022) − the various stages associated with the COVID-19 pandemic in Polokwane and Johannesburg; (ii) to use the extracted LSTs for Polokwane and Johannesburg to detect and interpret spatio-temporal changes in the UHIs and the non-UHIs of Polokwane and Johannesburg; (iii) to detect urban hot spots (UHSs) within the UHIs, and to perform dynamic analyses of them; and (iv) to analyse the correlations between the NDVI-NDBI-based LULC types and the LSTs for the two cities, respectively. The objectives of the current study are particularly relevant considering recent changes in urban dynamics.

The lockdowns triggered by COVID-19 have raised much interest and concern about the effects they have had on the different parts of metropoles/cities. Specifically, the impacts on the LSTs of different cities have had consequences for public health, environmental sustainability, and urban design. To reduce the detrimental effects of lockdowns on urban environments and increase the resilience and sustainability of cities, it is imperative to understand these effects. The analysis of the impact of the COVID-19-induced lockdown on LSTs offers valuable perspectives that can serve as a guideline in urban planning and policymaking processes, ultimately helping to build sustainable cities and communities. This is in line with Sustainable Development Goal (SDG) 11, which focuses on improving the sustainability of cities and communities.

2. Material and methods

2.1. Study area

The cities of Polokwane and Johannesburg in the Limpopo and Gauteng provinces respectively were selected as the study areas (Figure 1). Polokwane occupies a total area of 106.8 km^2, while Johannesburg covers 1645 km^2. Polokwane has mild to warm summers and cold, frosty winters (Tleane & Ndambuki, 2020). January is the hottest month, with the highest temperatures ranging from 26 to 28°C, whereas July is the coldest month, with temperatures ranging from 4 to 6°C (South African Weather Service, 2022). The annual rainfall ranges between 400 and 600 mm but is typically concentrated over only a short period of the year (South African Weather Service, 2022). On the other hand, the average annual temperature for Johannesburg is 20.6°C, with dry winters and wet summers (Jombo *et al*., 2022). Polokwane is home to a total human population of 463000 while Johannesburg accommodates 6065000 people (World Population Review, 2022).

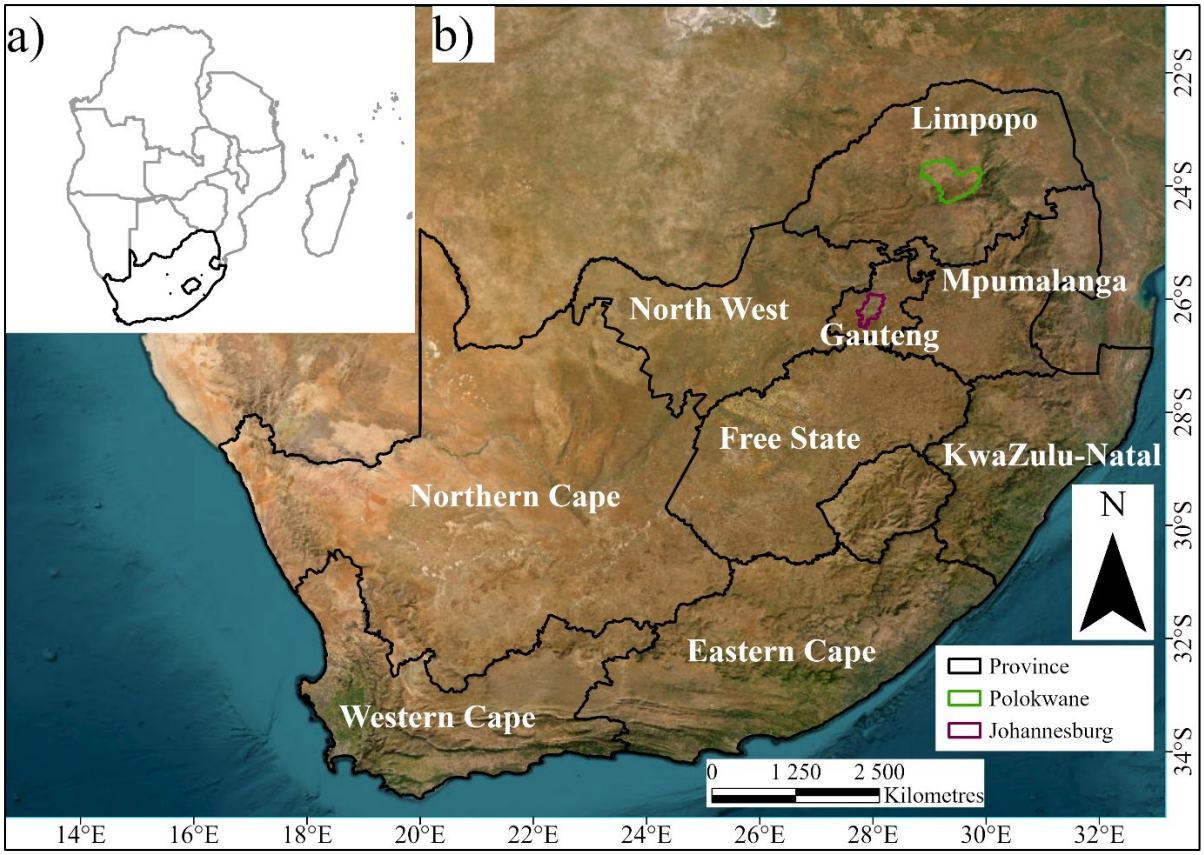

Figure 1: Map of a) Southern African countries and b) South African provinces highlighting Polokwane and Johannesburg.

2.2. Datasets

Landsat 8-9 operational land imager (OLI) and thermal infrared sensor (TIRS) satellite images were used to classify and calculate the land surface temperatures (LSTs) of the two cities. The satellite imageries (Table 1) were retrieved from the United States Geological Survey (USGS) Earth Explorer data interface at https://earthexplorer.usgs.gov/. The Landsat-8 and Landsat-9 imageries were collected in January 2021, March 2021, and April 2022 (Table 1).

Table 1: Specifications of Landsat 8-9 operational land imager (OLI) and Thermal Infrared Sensor (TIRS) data for Polokwane and Johannesburg.

Place	Satellite	Path/Row	Date of acquisition	Sun elevation (°)	Sun azimuth (°)	Scene cloud cover (%)
Polokwane	Landsat 8	170/077	17/01/2020	59	66	6.09
Polokwane	Landsat 8	170/077	08/03/2021	52	64	4.97
Polokwane	Landsat 9	170/077	12/04/2022	45	46	5.27
Johannesburg	Landsat 8	170/078	17/01/2020	59	87	4.38
Johannesburg	Landsat 8	170/078	08/03/2021	51	62	0.24
Johannesburg	Landsat 9	170/078	20/04/2022	42	42	7.50

At a pixel size of 30 m, the OLI acquires eight bands in the visible and near-infrared (VNIR) and shortwave infrared (SWIR) regions of the electromagnetic spectrum (EMS) (Table 2). It also acquires the panchromatic band at a pixel size of 15 m. The TIRS sensor detects a pixel size of 100 m in two bands between 10 and 12 µm of the EMS (Irons *et al*., 2012). The OLI data exhibit superior radiometric precision, thereby covering a dynamic range of 12 bits (Masek *et al*., 2020). Improved radiometric precision enhances the LULC classification to achieve high accuracies (Jallu *et al*., 2022). The band specifications for Landsat-8 and -9 are presented in Table 2.

Table 2: Band specification for Landsat 8 and 9 satellite imageries used in this study.

Region of the electromagnetic spectrum (EMS) and band number	Central wavelength (µm)	Resolution (m)
Coastal aerosol – Band 1	0.44	30
Blue – Band 2	0.48	30
Green – Band 3	0.56	30
Red – Band 4	0.65	30
Near-infrared (NIR) – Band 5	0.87	30
Shortwave infrared (SWIR) 1 – Band 6	1.61	30
Shortwave infrared (SWIR) 2 – Band 7	2.20	30
Panchromatic – Band 8	0.59	15
Cirrus – Band 9	1.37	30
Thermal Infrared Sensor (TIRS) 1 – Band 10	10.90	100
Thermal Infrared Sensor (TIRS) 2 – Band 11	12.01	100

2.3. Data pre-processing

The LST values were derived from the Landsat 8 and 9 images. The image preprocessing involved radiometric calibration, surface emissivity calculation, and a thermal band conversion. Equation 1 was used to convert the data from the OLI and TIRS bands to spectral radiance.

$$L_\lambda = M_L \times Q_{cal} + A_L \qquad [1]$$

where L_λ represents the apparent spectral radiance at the top of the atmosphere (TOA) ($Wm^{-2}sr^{-1}\mu m^{-1}$), M_L and A_L are band-wise multiplicative and additive rescaling factors, respectively, and Q_{cal} stands for the quantized/calibrated standard digital number (DN) values (NASA, 2022). Through the application of Equation 1, radiance images were generated for bands 10 of the OLI and TIRS datasets.

An improved image-based dark object subtraction (DOS) model (Equation 2) was applied to eliminate low reflection values attributed to air diffusion (Adeyeri *et al*., 2017; Chavez, 1996).

$$L_1P = L_1min - L_1(DO1\%) \qquad [2]$$

where L_1min is the radiance of the minimum DN value of the image ($Wm^{-2}sr^{-1}\mu m^{-1}$), and $L_1(DO1\%)$ represents the radiance of the dark object (DO) ($Wm^{-2}sr^{-1}\mu m^{-1}$) (Adeyeri *et al*.,

2017). Only band 10 (TIRS1) was used because it performed better than band 11 (TIRS2) (Adeyeri *et al*., 2017).

2.4. Calculation of LSTs

The two essential inputs for the retrieval of LSTs from the Landsat thermal dataset were the surface emissivity and the at-sensor brightness temperature (BT) estimates. The TIRS data underwent a conversion from spectral radiance to BT through the application of the following equation (USGS, 2019). Assuming unity emissivity, BT represents the effective temperature observed by the satellite.

$$BT = \frac{K2}{Ln\left(\frac{K1}{L_\lambda}+1\right)} - 273.15 \qquad [3]$$

where BT is the TOA brightness temperature, measured in Kelvin (K), $K1$ and $K2$ represent the pre-launch calibrations of band 10 — from the metadata, Ln stands for the natural algorithm, and L_λ is the TOA spectral radiance ($Wm^{-2}sr^{-1}\mu m^{-1}$) in Equation 1. The value of 273.15 was subtracted from the BT to convert K to degrees Celsius (°C). This study used only band 10 (TIRS1) because band 11 (TIRS2) exhibited major calibration uncertainties (Department of the Interior United States Geological Survey, 2019) that could have led to inaccurate results. Owing to calibration and stray light issues, band 10 instead of band 11 was used in our study, as analyses showed that band 11 exhibited more substantial banding effects and absolute calibration errors, primarily attributed to stray light (Montanaro *et al*., 2014).

Vegetation greenness, well captured using NDVI, revealed plant and biomass conditions (Purevdorj *et al*., 1998). For the NDVI calculation, bands 4 and 5 of the satellite imageries were used, producing values ranging between -1 and +1. Areas with less or no vegetation presented with values close to -1 and *vice versa*. Calculating the NDVI helped the researchers to better understand vegetation patterns in urban areas and allowed for the computation of surface emissivity (ε) (Sobrino *et al*., 2001; Sobrino *et al*., 2004).

Therefore, NDVI calculation was necessary for approximating vegetation cover and computing surface emissivity (ε):

$$NDVI = \frac{\rho NIR - \rho Red}{\rho NIR + \rho Red} \qquad [4]$$

where ρNIR and ρRed stand for the reflectance of the NIR and Red bands, respectively.

The NDVI values obtained in Equation 4 were employed to calculate vegetation cover:

$$P_v = \left(\frac{NDVI - NDVI_{min}}{NDVI_{max} - NDVI_{min}}\right)^2 \qquad [5]$$

Where P_v is the fractional vegetation cover, and $NDVI_{min}$ and $NDVI_{max}$ denote minimum and maximum NDVI values, respectively.

Land surface emissions show the percentage of radiance emitted by a body at a given temperature and the radiance released by a blackbody at an equivalent temperature (Tarawally *et al*., 2018). The P_v values were used to compute the land surface emissivity(ε):

$$\varepsilon = 0.004^{*}P_v + 0.986 \qquad [6]$$

where P_v represents the proportion of vegetation[1].

Using ε and BT, it was possible to compute the LST for band 10 using the equation devised by Stathopoulou & Cartalis (2007) and Weng *et al*. (2004):

$$LST = \frac{BT}{\left(1+\left[\left(\frac{\lambda BT}{\rho}\right)ln\varepsilon\right]\right)} \qquad [7]$$

where BT represents the brightness temperature, ρ stands for $1.438{*}10^{-2}$mk, λ represents band 10, and ln and ε denote the natural logarithm and land surface emissivity, respectively.

It was therefore possible to retrieve the respective LST maps for the years 2020, 2021, and 2022.

2.5. Detection of UHIs and non-UHIs

The range of LST values in each of the study areas contributed to the identification of the UHIs and non-UHIs in Polokwane and Johannesburg (Guha *et al*., 2017; Ma *et al*., 2010). Generally, the detection of UHIs and non-UHIs is made possible by examining the temperature patterns that prevail in urbanised and non-urbanised areas. Underlying UHIs occur in parts of cities where urbanisation and human activity cause temperatures to rise noticeably above those of the nearby rural areas (Adeyeri *et al*., 2017). In this study, the UHIs and non-UHIs were determined by applying the following equations:

$$LST > \mu + 0.5^{*}\delta \qquad [8]$$

$$0 < LST \leq \mu + 0.5^{*}\delta \qquad [9]$$

where μ and δ represent the mean and standard deviation values for the LSTs in question.

2.6. Mapping the Urban Heat Spots (UHSs)

The LST maps were used to identify the UHSs within the UHIs over Polokwane and Johannesburg respectively (Guha *et al*., 2017):

$$LST > \mu + 2^{*}\delta \qquad [10]$$

The hotspots were employed to extract the corresponding pixel values for Inverse Distance Weighting (IDW) interpolation, thereby creating a rasterised map to illustrate the spatial distribution of the LSTs for these hotspots.

[1] 0.004 and 0.986 are thresholds derived from Sobrino *et al*. (2004).

2.7. Generation of LULC maps using NDVI and NDBI

The study used two spectral indices, the NDVI (Tucker, 1979; Purevdorj *et al*., 1998) and the NDBI (Zha *et al*., 2003) to analyse and assess the data. The indices were calculated from the OLI datasets for 2020, 2021, and 2022 to represent the LULC types. The values of the two indices were between −1 and +1. Positive values indicate the presence of vegetation for NDVI and of built-up areas for NDBI, whereas negative values signify the existence of other LULC classes (Mishra & Garg, 2023). NDVI typically employs bands scaled to reflectance values as inputs, whereas NDBI uses bands expressed in DN (Mishra & Garg, 2023). Relational operators (>, <) were applied for accurate classification results (i.e., vegetation extraction involved the use of NDVI values > 0.2 and NDBI values < 0, whereas the detection of water bodies employed NDVI and NDBI values < 0. The criteria for identifying built-up areas, roads, and bare land included NDVI values between 0 and 0.2, along with NDBI values greater than 0.1.[2] The false colour composites (FCCs) for 2020, 2021, and 2022 were created by combining bands 5, 4, and 3. These FCCs were overlaid onto higher-resolution Google Earth imagery captured at the exact date and time of the OLI data acquisition. Using the visual interpretation skills and the regions of interest (ROIs), representing the various LULC types, the relevant waterbodies, bare land, built-up areas, roads, and vegetation were digitised. The ROIs were overlaid to serve as signatures for training the support vector machine (SVM) classification algorithm — this algorithm requires only a few training data samples (Mushore *et al*., 2017). The ROIs served as the ground truth for accuracy assessment. To generate LULC maps, the ground truth data were randomly split as follows: 70% for classification and 30% for validation.

The NDBI was computed by applying the equation:

$$NDBI = \frac{\rho SWIR - \rho NIR}{\rho SWIR + \rho NIR} \qquad [11]$$

where $\rho SWIR$ and ρNIR represent surface reflectance for band 6 and band 5.

2.8. Accuracy assessment

Thirty per cent (30%) of the ground truth data was used to generate confusion matrices to determine the level of accuracy and reliability of the created LULC maps. The overall accuracy, producer's and user's accuracies, and kappa were used in the process. The user's accuracy represents the likelihood that a sample belongs to a particular class, to the effect that the classifier accurately assigns it to that class. In contrast, the overall accuracy metric is a ratio (%) between the number of successfully categorised samples and the number of test samples (Jombo *et al*., 2020). The producer's accuracy indicates the frequency with which actual features on the ground are accurately represented on the classified map. The kappa coefficient

[2] According to Chen *et al*. (2006), these values can be integrated for LULC classification.

was calculated to assess the agreement between the classified and ground truth samples (Jombo *et al*., 2020).

2.9. Estimation of LST patterns and statistics per LULC class

To enhance the researchers' comprehension of the correlation between LULC changes and LST, 50 points were chosen for analysis. These points were distributed across the study areas and represented 10 points for each LULC class. The goal was to examine how different LST patterns relate to different types of land cover or how changes in LST can be used to track land use changes. A representative number of points from each LULC class was selected to capture a range of LST values across the study areas. This approach allows for a better understanding of the underlying factors driving LST changes in different parts of the study areas and identifies potential drivers of observed changes in LST over time. By examining LST patterns at the point scale, this study was able to gain insights into the spatial variability of LSTs and to understand how LULC and LST are related.

2.10 Correlation analysis for assessing the associations/correlations between the selected spectral indices and LST

Pearson's correlation analysis was performed to examine the associations between NDVI, NDBI, and LST (Emerson, 2015):

$$r = \frac{\Sigma(x_i - \bar{x}) - \ (y_i - \bar{y})}{\sqrt{\Sigma(x_i - \bar{x})^2 - \Sigma(y_i - \bar{y})^2}} \quad [12]$$

where r denotes the Pearson's correlation coefficient, with x_i and y_i representing the values of the respective x and y variables. The symbols $\bar{x}$ and $\bar{y}$ denote the mean values of the respective x and y variables (Wiedermann & Hagmann, 2016). A correlation coefficient of 0 indicates no linear correlation, while a coefficient closer to +1 or -1 indicates a stronger linear correlation. Using Pearson's correlation analysis in this study allowed for a more precise evaluation of the relationship between these variables. It provided valuable information for understanding the impact of LULC changes on LST. Furthermore, the selection of 50 points for analysis ensured a representative sample size and enhanced the statistical significance of the findings.

3. Results

3.1. Spatio-temporal dynamics of NDVI, NDBI, and LST

Table 3 presents the descriptive statistics for the NDVI, NDBI and LST values. The descriptive statistics reveal the dynamic nature of the spectral indices and LST between 2020 and 2022, with notable differences before, during, and after the COVID-19 pandemic. In

Polokwane, there was an increase in the mean NDVI values from 0.25 in 2020 to 0.32 in 2021 (Table 3) but a decline to 0.29 in 2022 (post-pandemic) (Table 3). However, there was a decline in the mean LST value from 31.2°C in 2020 (pre-pandemic) to 25.55°C in 2021 (during the pandemic), followed by an increase to 28°C in 2022 (post-pandemic) (Table 3). The mean NDVI values in Johannesburg increased from 0.31 in 2020 to 0.39 in 2021 and decreased to 0.26 in 2022 (Table 3). The mean NDBI values increased from 0.11 in 2020 to 0.18 in 2022, while LST recorded the highest mean value of 32.40°C in 2020, a decline to 28.35.8°C in 2021, and an increase to 31.35°C in 2022 (post-pandemic) (Table 3).

Predominantly, in 2020 (pre-pandemic), the highest NDBI values prevailed in the southern and eastern regions of the study area in Polokwane (Figs. 2d-f), with LST being widely spread across the area (Fig. 2g). Figure 2 shows the NDVI, NDBI, and LST values for Polokwane and Johannesburg in 2020, 2021, and 2022, respectively. LST distributions were categorised into suitable ranges and colour coded as illustrative thermal pattern distribution maps for the study areas. To validate the LST values depicted on the maps, the in-situ temperature data obtained for Polokwane and Johannesburg from the South African Weather Services (SAWS), were used. The in-situ temperature data strongly correlated with the LST values in both study areas, with R2 values ranging from 0.79 to 0.88 between January 2020 and April 2022.

Table 3: Descriptive statistics for NDVI, NDBI, and LST for a) Polokwane and b) Johannesburg (2020, 2021, and 2022).

Polokwane				
NDVI				
Year	Minimum	Maximum	Mean	Standard deviation
2020	-0.1	0.60	0.25	0.18
2021	-0.1	0.74	0.32	0.14
2022	-0.1	0.67	0.29	0.13
NDBI				
	Minimum	Maximum	Mean	Standard deviation
2020	-0.4	1	0.3	0.23
2021	-0.1	1	0.45	0.18
2022	0	1	0.5	0.17
LST				
	Minimum	Maximum	Mean	Standard deviation
2020	19.8	42.6	31.2	0.8
2021	13.6	37.5	25.55	1.98
2022	17.6	38.4	28	0.47
Johannesburg				
NDVI				
	Minimum	Maximum	Mean	Standard deviation
2020	0.15	0.63	0.31	0.15
2021	-0.07	0.69	0.39	0.13
2022	-0.1	0.61	0.26	0.12
NDBI				
	Minimum	Maximum	Mean	Standard deviation
2020	-0.52	0.78	0.11	0.22
2021	-0.75	0.81	0.15	0.26
2022	0.12	0.84	0.18	0.12
LST				
	Minimum	Maximum	Mean	Standard deviation
2020	20.8	44	32.4	1.07
2021	17.9	38.8	28.35	0.13
2022	22.4	40.3	31.35	0.97

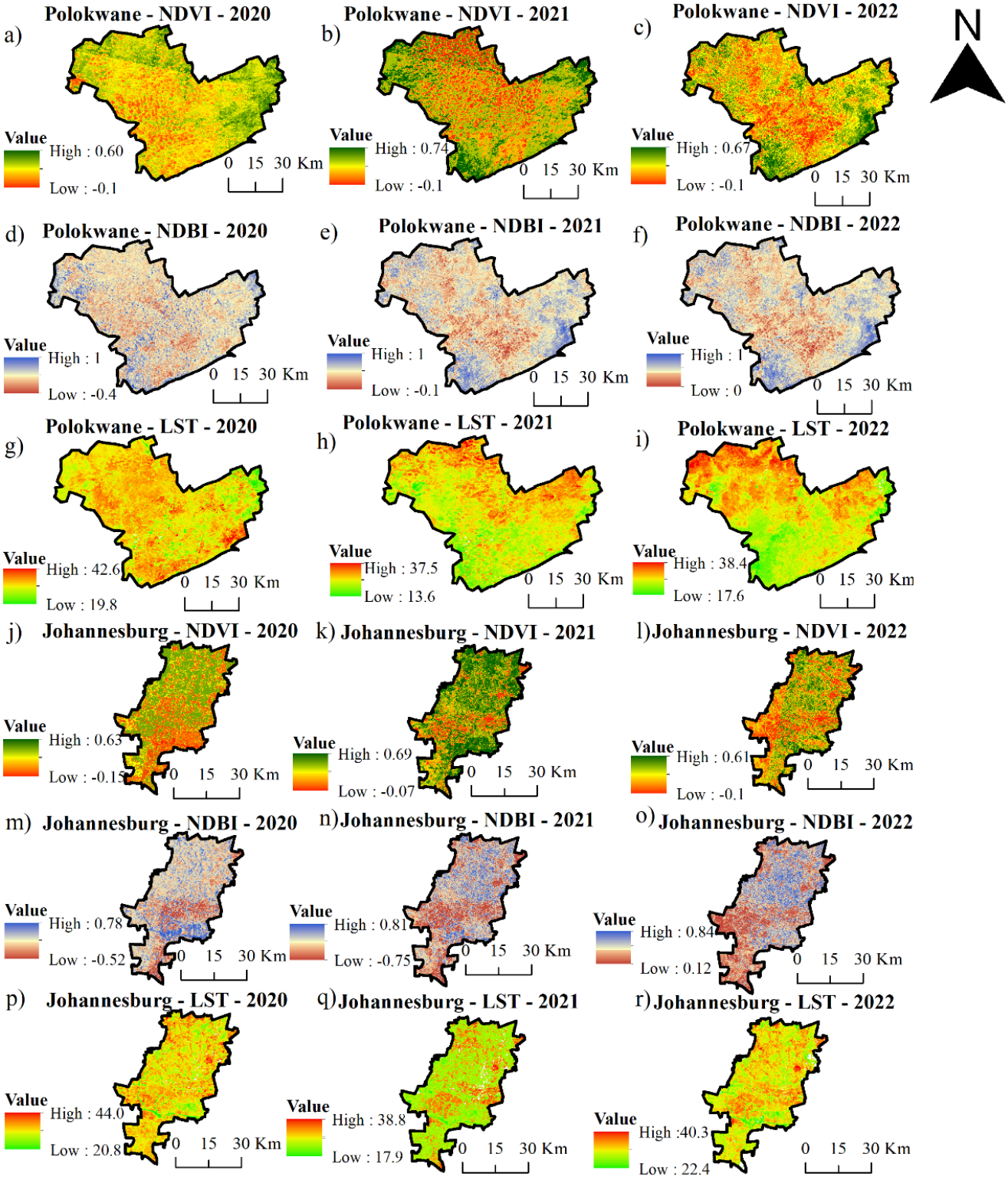

Figure 2: Maps showing the Normalized Difference Vegetation Index (NDVI), the Normalized Difference Built-up Index (NDBI), and Land Surface Temperatures (LSTs) for Polokwane and Johannesburg in 2020, 2021, and 2022, respectively.

3.2. Spatio-temporal distribution of UHIs and non-UHIs

The comparison between the mean LST values in UHIs and non-UHIs was used to determine the intensity of the UHI effect. Table 4 presents the findings for the years 2020,

2021, and 2022 for Polokwane and Johannesburg. In Polokwane, there was a mean LST difference of 6.22°C, 8.09°C, and 6.33°C between UHI and non-UHI areas for the respective years (Table 4). Similarly, in Johannesburg, the mean LST differences between UHIs and non-UHIs were 6.14°C, 5.88°C, and 3.83°C, for the respective study years. Notably, the UHI effect in Polokwane presented a 2.30°C decrease from 2020 to 2021, while Johannesburg saw a decrease of 3.78°C during the same period (Table 4). Conversely, non-UHI areas in Polokwane and Johannesburg experienced decreases of 4.17°C and 3.32°C, respectively, from 2020 to 2021 (Table 4). In Johannesburg, UHI areas predominantly occur in the southern part of the city, contrasting with the non-UHI areas which are concentrated in the northern part (Figure 3). The UHI threshold temperatures for 2020 were 42.6°C for Polokwane and 44°C for Johannesburg (Table 4).

Table 4: Temporal LST (°C) variations between UHIs and non-UHIs.

a) Polokwane								
	LST (min)		LST (max)		LST (mean)		LST (SD)	
Year	UHI	Non-UHI	UHI	Non-UHI	UHI	Non-UHI	UHI	Non-UHI
2020	25.4	19.8	42.6	35.11	32.14	25.92	0.81	1.24
2021	23.6	13.6	37.5	32.52	29.84	21.75	0.64	1.11
2022	25.8	17.6	38.4	34.35	30.05	23.72	0.71	1.22
b) Johannesburg								
	LST (min)		LST (max)		LST (mean)		LST (SD)	
Year	UHI	Non-UHI	UHI	Non-UHI	UHI	Non-UHI	UHI	Non-UHI
2020	25.2	20.8	44	35.24	32.77	26.63	0.74	1.33
2021	23.5	17.9	38.8	32.11	28.99	23.31	0.64	0.92
2022	24.6	22.4	40.3	34.76	30.68	26.85	1.12	1.56

3.3. Spatio-temporal mapping of Urban Hotspots (UHSs)

Developed within the UHIs of the two study areas, the UHSs were mapped for continuous monitoring over the years of study. The UHIs with high LST values are primarily located in the northern part of Polokwane (Figs. 3a-c) and were found to have little vegetation and a high built-up structure density. Conversely, in Johannesburg, the UHIs with their high LST values are predominantly found in the southern part of the city (Figs. 3d-f).

A threshold of 35°C was applied to identify UHIs in Polokwane and Johannesburg, respectively. The manufacturing industry, transport sector, power generation infrastructures or installations, and their related activities, and built-up areas − especially buildings with metal roofs, bare land, and exposed rocks, were recognised as the most prolific land use classes in the context of UHSs (Guha *et al*., 2018). Therefore, land conversions from vegetation or water bodies to bare land or built-up areas, together with the pollution of the surrounding atmosphere

in such areas, were identified as major factors for generating UHSs in Polokwane and Johannesburg.

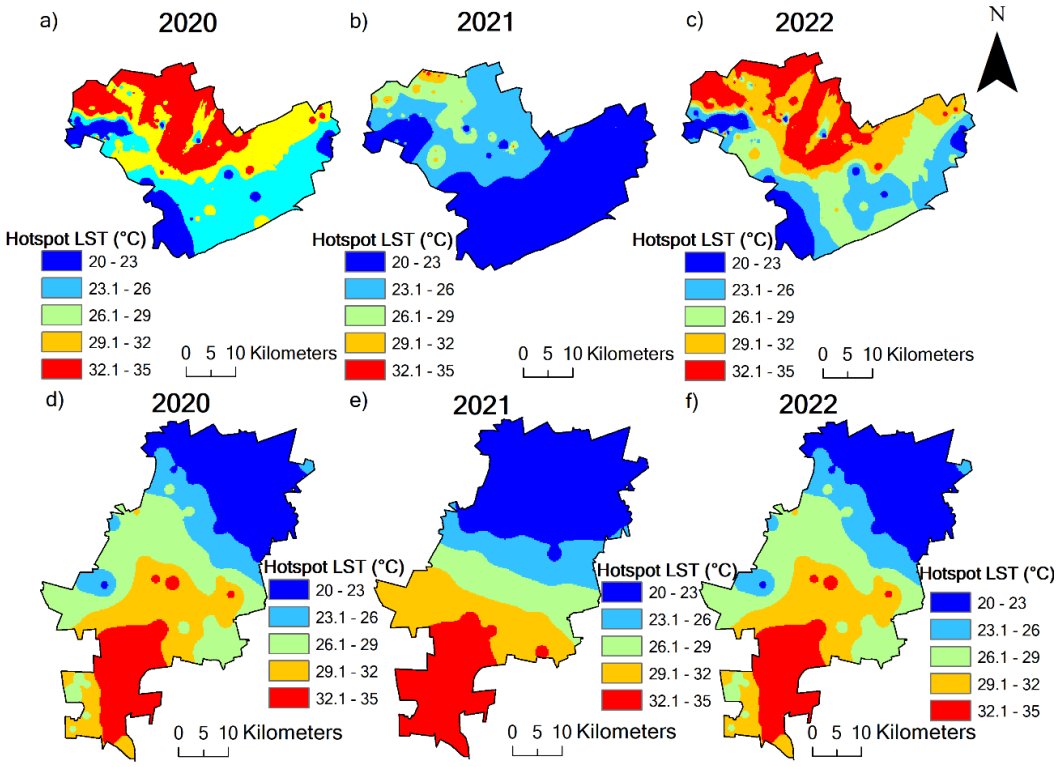

Figure 3: Land surface temperature (LST) hotspots for Polokwane (a-c) and Johannesburg (d-f) in 2020, 2021 and 2022, respectively.

3.4. Analysis of LULC maps generated using NDVI and NDBI

Figure 4 shows the spatio-temporal distribution of LULC indices (NDVI and NDBI). The area classified as built-up is situated mainly in the northern part of Polokwane (Figs. 4a-c). Vegetation predominates in the central area of Polokwane, while waterbodies occupy only a small section of the city (Figs. 4a-c). In Johannesburg, vegetation is widely spread across the northern side of the city (Figs. 4d-f). Built-up areas and bare land are mainly located in the south, and there is only a small area of coverage by waterbodies and roads (Figs. 4d-f).

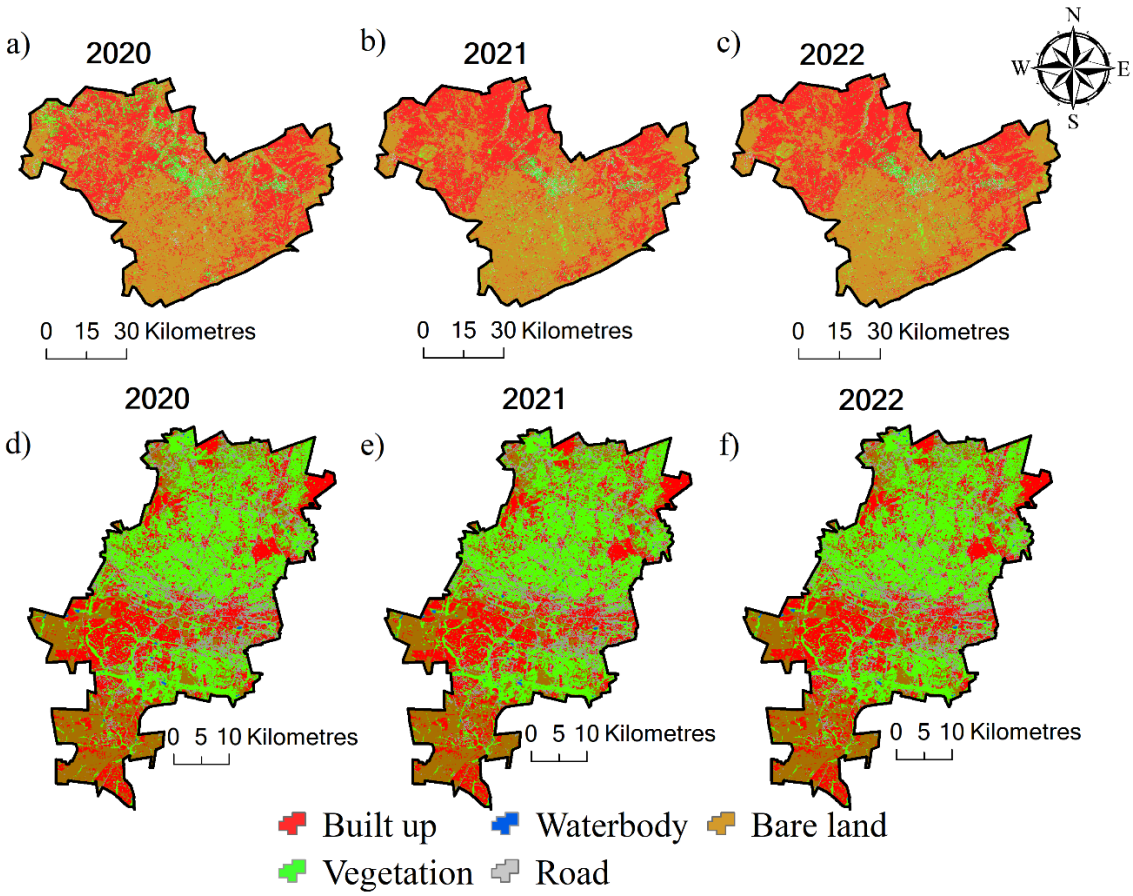

Figure 4: Land use/land cover (LULC) maps for Polokwane in a) 2020, b) 2021, and c) 2022, and LULC maps for Johannesburg in d) 2020, e) 2021, and f) 2022.

3.5. Validation of LULC maps

As shown in Figure 5, the overall accuracies for the LULC maps for Polokwane ranged between 89 (2020) and 94% (2022). The producer's accuracies ranged from 82 to 100% for the three satellite imageries, while the user's accuracies ranged between 80 and 100%.

As indicated in Figure 6, the overall accuracies for the LULC maps for Johannesburg varied between 90% in 2020 and 95% in 2022. Regarding the three satellite imageries, the producer's accuracies were in the range of 90-100%, and the user's accuracies ranged from 88 to 100% (Figure 6).

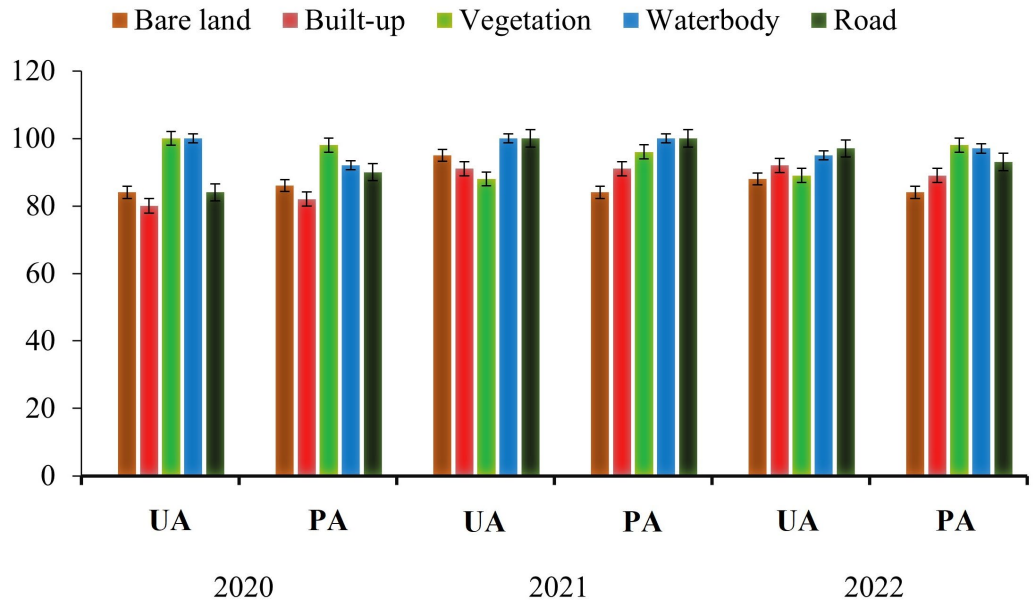

Figure 5: User's accuracy (UA), producer's accuracy (PA) and overall accuracy (OA) values for Polokwane in 2020, 2021, and 2022.

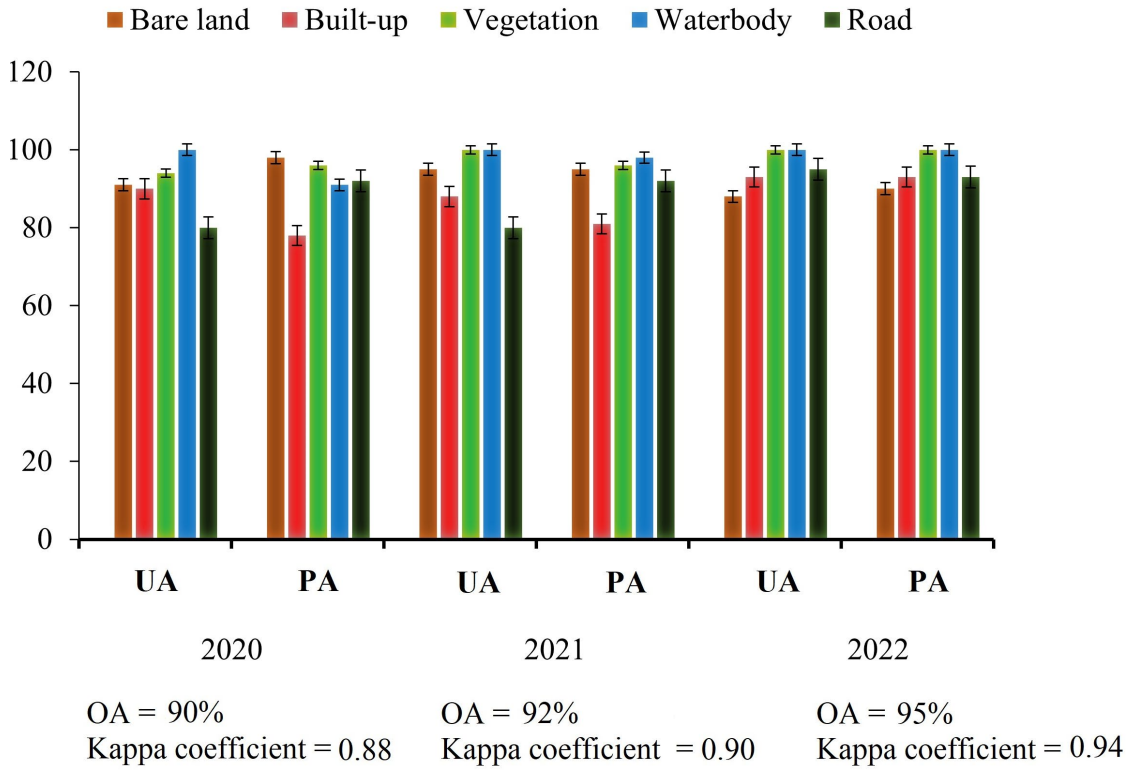

Figure 6: User's accuracy (UA), producer's accuracy (PA), and overall accuracy (OA) values for Johannesburg in 2020, 2021 and 2022.

3.6. The association between the distribution of LULC classes and the distribution of LSTs

High LST values were observed for all LULC classes in 2020, before the COVID-19 pandemic. The values were 38°C, 36°C, 32°C, 26°C and 24°C for the bare land, built-up, road, vegetation and waterbody classes, respectively (Figure 7). The lowest LST values were recorded in Polokwane during the pandemic in 2021 (Figure 7). These values were 32°C, 30°C, 29°C, 20°C and 18°C for the bare land, built-up, road, vegetation and waterbody classes, respectively (Figure 7). The distribution plots for LST for LULC classes for Polokwane that were used in this study before, during, and after the COVID-19 lockdown in 2020, 2021, and 2022, respectively, are shown in Figure 7.

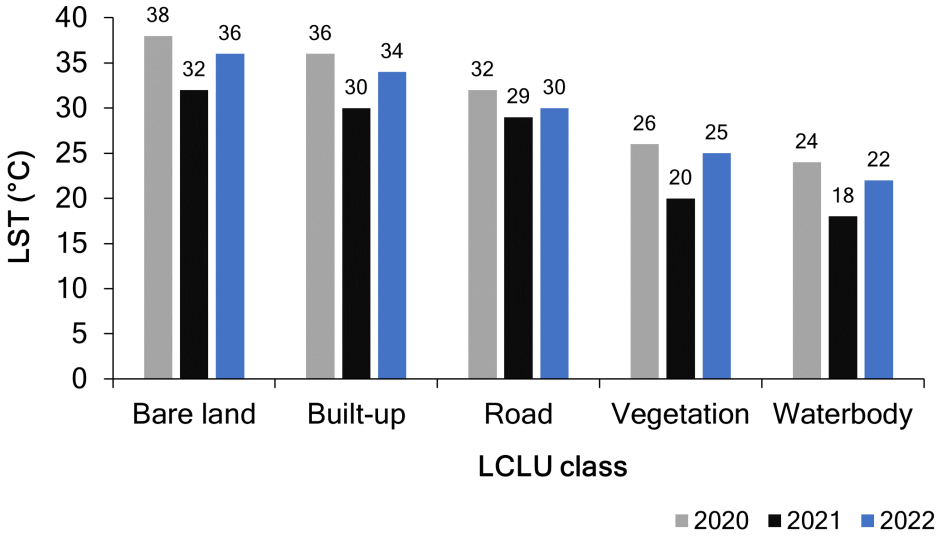

Figure 7: Land use/land cover (LULC) classes and land surface temperatures (LSTs) in degrees Celsius (°C) for Polokwane in 2020, 2021 and 2022.

The highest LST value (32.6°C) for Polokwane was recorded for the built-up class in 2020, while the lowest value (19.7°C) was for the waterbody class in 2021, during the lockdown (Table 5). A rise in LST values for all LULC classes was observed from 2021 (during lockdown) to 2022 (after lockdown), with the most significant increase of 1.9°C being for the bare land class (Table 5). These outcomes highlight the beneficial effects of the lockdown in Polokwane.

The distribution plots for LSTs in terms of the LULC classes used in this investigation before, during, and after the COVID-19 lockdown in Johannesburg in 2020, 2021, and 2022, respectively, are displayed in Figure 8. Before the COVID-19 pandemic, all LULC classes in Johannesburg presented with high LST values. As shown in Figure 8, the LST values were 38°C for bare land, 37°C (built-up), 34°C (road), 25°C (vegetation) and 21°C (waterbody). The

lowest values were recorded during the pandemic in 2021 (Figure 8). The lowest value for all LULC classes was 16°C for waterbodies (Figure 8).

Table 5: Mean land surface temperatures (LSTs) in degrees Celsius (°C) for Polokwane in 2020, 2021 and 2022.

	Mean land surface temperature (LST) in degrees Celsius (°C)		
Class	January 2020	March 2021	April 2022
Bare land	24.7	21.3	23.2
Built-up	32.6	30.4	31.2
Road	27.4	26.2	26.7
Vegetation	25.4	22.1	23.4
Waterbody	21.2	19.7	20.3

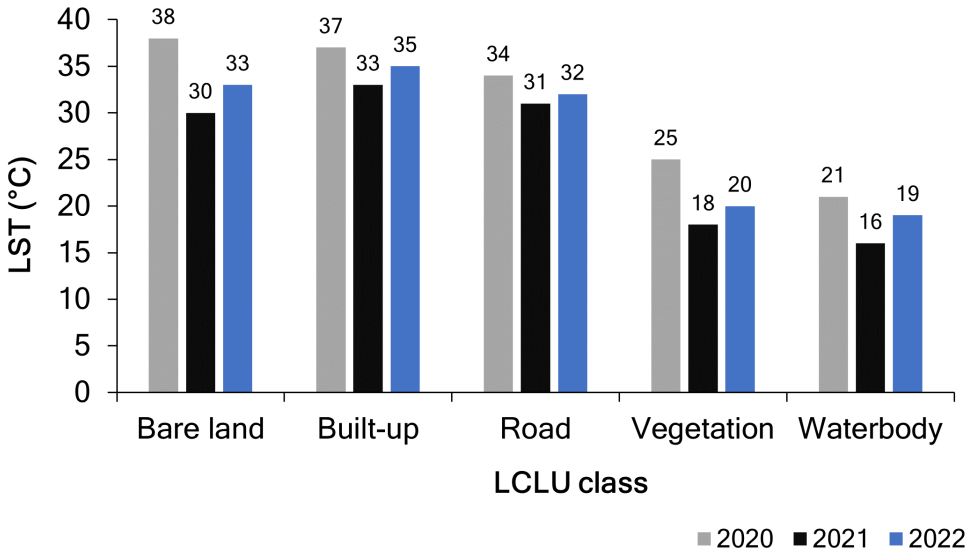

Figure 8: Land use/land cover (LULC) classes and land surface temperatures (LSTs) in degrees Celsius (°C) for Johannesburg in 2020, 2021 and 2022.

The LST values before, during, and after the COVID-19 lockdown in Johannesburg are shown in Table 6. The highest LST value for Johannesburg in 2020 was 34.6°C for built-up, followed by 25.6°C (road) (Table 6). The LST values for all LULC classes increased in 2022 (after the lockdown) (Table 6). Between 2021 and 2022, the highest LST increase was 1.3°C for vegetation, while the lowest increase was 0.3°C for the road class (Table 6).

Table 6: Mean land surface temperatures (LSTs) in degrees Celsius (°C) for Johannesburg in 2020, 2021, and 2022.

	Mean land surface temperature (LST) in degrees Celsius (°C)		
Class	January 2020	March 2021	April 2022
Bare land	19.6	18.6	19.2
Built-up	34.6	33.1	33.5
Road	25.6	24.6	24.9
Vegetation	25.4	22.1	23.4
Waterbody	20.2	19.5	19.9

3.7. Relationship between LULC indices and LST

The study employed Pearson's correlation analysis, with a significance level of 95% (p-value < 0.05), to examine the respective associations between NDVI and LST and between NDBI and LST in the study areas. Table 7 shows the relationships between the LULC indices for Polokwane in 2020, 2021 and 2022, respectively. There was typically a negative correlation between NDVI and LST, while a positive correlation was observed between NDBI and LST: − In 2020, LST was negatively correlated to NDVI with a value of -0.62, while positively correlated to NDBI with a value of 0.81 (Table 7). Similarly, LST was negatively correlated to NDVI in 2021 and 2022, with values of -0.58 and -0.71, respectively (Table 7).

Table 7: Correlation coefficients for the three indices (NDVI, NDBI and LST) for Polokwane in 2020, 2021 and 2022.

	NDVI	**NDBI**	**LST**
	2020		
NDVI	1		
NDBI	-0.25	1	
LST	-0.62	0.81	1
	2021		
NDVI	1		
NDBI	-0.04	1	
LST	-0.58	0.79	1
	2022		
NDVI	1		
NDBI	-0.01	1	
LST	-0.71	0.85	1

Table 8 displays the correlation coefficients for NDVI and LST for Johannesburg in 2020, 2021, and 2022, respectively. A negative correlation was observed in all three years, with respective coefficient values of -0.69, -0.69, and -0.73. Likewise, Table 8 demonstrates that NDVI and NDBI are negatively correlated, featuring correlation coefficients of -0.33, -0.24, and -0.36. As indicated in Table 8, a positive correlation was observed between NDBI and LST with respective coefficient values of 0.70, 0.59, and 0.77.

The linear regression model was applied to investigate the impact of NDVI and NDBI on fluctuations in LSTs. The spectral indices (NDVI and NDBI) were regarded as the independent variables, and LST as the dependent variable. The R^2 and p-values allowed for the interpretation of the outcomes of the analysis. Figures 9 and 10 show the results of the models and the regression analysis equations for Polokwane and Johannesburg, respectively. Generally, the linear regression models show that the influence of NDVI and NDBI on LST varied over the study periods: In 2020, there was a negative correlation of -0.22 between NDVI and LST in Polokwane, thus indicating an inverse association between the two variables. On the other hand, however, as depicted in Figure 9c, there was a positive correlation of 0.11 between NDBI and LST in Polokwane. Similarly, in 2021, negative correlations were found between NDVI-LST (-0.17) and NDBI-LST (-0.023) (Figs. 9e and 9f, respectively). A negative correlation of -0.11 was observed in 2022 between NDVI and LST (Fig. 9h), while a positive correlation of 0.20 was found between NDBI and LST (Fig.9i). These findings highlight the relationships amongst all indices (NDBI, NDVI and LST) in Polokwane during the pre-COVID-19 pandemic (2020), the pandemic period (2021), and the post-pandemic period (2022).

Table 8: Correlation coefficients for the three indices (NDVI, NDBI and LST) for Johannesburg in 2020, 2021 and 2022.

	NDVI	**NDBI**	**LST**
	2020		
NDVI	1		
NDBI	-0.33	1	
LST	-0.69	0.70	1
	2021		
NDVI	1		
NDBI	-0.24	1	
LST	-0.69	0.59	1
	2022		
NDVI	1		
NDBI	-0.36	1	
LST	-0.73	0.77	1

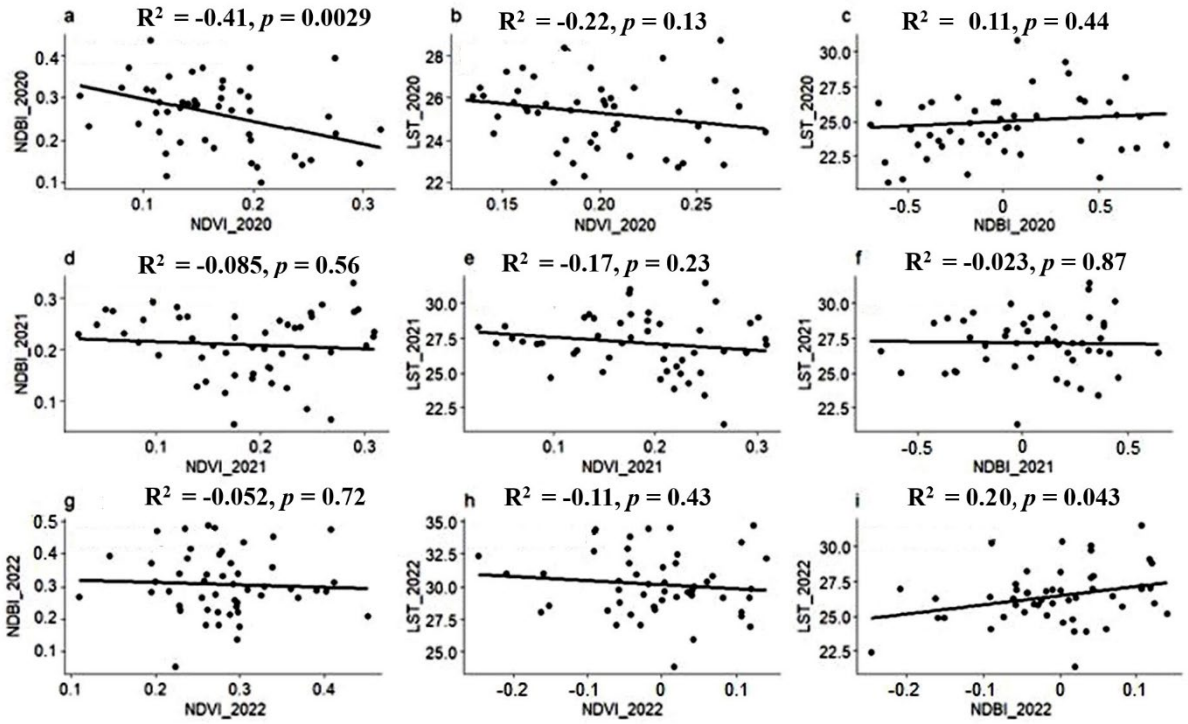

Figure 9: Linear regression analyses between NDVI, NDBI, and LST for Polokwane in 2020, 2021 and 2022.

As depicted in Figure 10b, in the case of Johannesburg in 2020, a negative correlation of -0.69 was observed between NDVI and LST, thus indicating an inverse association between the two variables. Conversely, as depicted in Figure 10c, a positive correlation of 0.79 was found between NDBI and LST in Johannesburg. Similarly, in 2021, significant negative correlations were discovered between NDVI-NDBI (-0.57) and NDVI-LST (-0.58) and (Figs. 10d and 10e, respectively. A negative correlation of -0.41 was observed in 2022 between NDVI and LST, while a positive correlation of 0.46 was identified between NDBI and LST, as illustrated in Figs 10h and 10i. These compelling findings underscore the interrelationships among all indices (NDVI, NDBI and LST) in Johannesburg throughout the pre-COVID-19 pandemic (2020), the pandemic period (2021), and the post-pandemic period (2022).

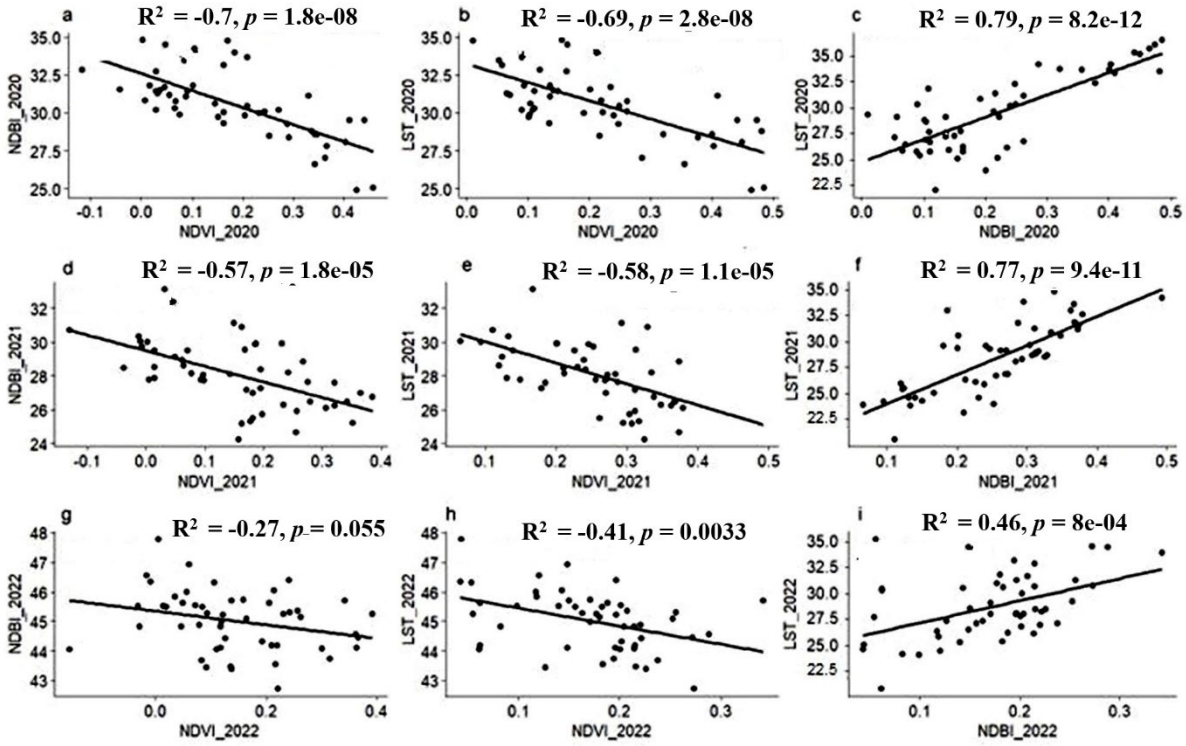

Figure 10: Linear regression analyses between NDVI, NDBI, and LST for Johannesburg in 2020, 2021, and 2022.

4. Discussion

The study assessed how the COVID-19 lockdown affected LSTs in Polokwane and Johannesburg. The LST values in the study areas before (January 2020), during (March 2021) and post (April 2022) COVID-19 pandemic were retrieved from Landsat images. The retrieved LSTs for the study areas were used to detect and interpret the spatio-temporal changes in UHIs and non-UHIs. UHSs were detected within the UHIs and correlations between the NDVI-NDBI-based LULC types and LSTs were analysed in the study areas. The LST values for the two cities declined amid the COVID-19 lockdown. The maximum LST values in Polokwane and Johannesburg decreased by 5.1°C and 5.2°C, respectively. These findings concur with those of Jallu *et al*. (2022), who identified a decrease in LSTs by 5°C in New Delhi, 1.9°C (Hyderabad), and 0.26°C (Mumbai) in April 2020. The decline in the LST values in these cities was due to reduced vehicular traffic, an improvement in the quality of the air, and the closure of industries because of lockdowns in India during the Covid-19 pandemic. Similarly, Zambrano-Monserrate *et al*. (2020) established a robust correlation between lockdowns and improvements in the quality of air and reduced noise levels.

Built-up areas generally presented with higher LST values during and after the COVID-19 lockdown period. This was due to their high radiant heat transfer levels. These results agree with those of Mushore *et al*. (2017), who indicated that built-up areas have high LSTs, with

substantial radiant heat transfers resulting from the transfer of relatively low latent heat. As indicated by the LULC maps of Polokwane and Johannesburg, high LST values were found in places with high-rise buildings and densely populated areas with little vegetation cover. Such conditions result from the prevalence of built structures, which obstruct the role of winds and air currents in ventilation. Furthermore, bare land areas and open spaces are generally unable to absorb solar radiation (Mushore *et al*., 2017; University Corporation for Atmospheric Research, 2011). Mudede *et al*. (2020) revealed that tall structures also present rougher surfaces, which hinder the transfer of heat through convection and radiative cooling. These authors also drew attention to the fact that bare soils are ineffective in absorbing solar radiation, which in turn raises LSTs.

Increased population numbers in Polokwane and Johannesburg have led to vegetational losses as people tend to clear the land of its natural vegetation to cater for their growing demand for accommodation which in turn results in high LSTs. Njoku and Edokpayi (2022) revealed that the population in Polokwane is growing at a rate of 3.27% annually, with internal migration increasing by 1.7%. Similarly, Jombo *et al*. (2022) indicated that the increase in the population numbers in Johannesburg has caused an escalation in the demand for housing and the loss of vegetational cover, both of which also result in high LST values.

During the years covered by this study, relatively lower temperatures were recorded in the waterbodies and vegetated areas of Polokwane and Johannesburg. Owing to their propensity to be porous and therefore to absorb heat, these areas presented with lower temperatures and thus served as heat sinks. This study found that the temperatures in vegetated areas and waterbodies were lower during the COVID-19 lockdown because of the reduction in emissions emanating from human activities. Vegetational growth and improved water quality were thus positive outcomes of the lockdowns. Su *et al*. (2021) support this claim by pointing out that during the COVID-19 pandemic, anthropogenic emissions were reduced, thereby resulting in lower aerosol optical depth (AOD) levels, thus influencing radiation levels and the growth of vegetation. A further reduction in water pollution during the COVID-19 lockdown period improved the absorptive capacity of water bodies and kept the environment cooler. This was because water bodies act as heat sinks. Chakraborty *et al*. (2021) indicated that during the COVID-19 lockdown, the total cessation of industrial activity, mining, and commercial operations played a pivotal role in enhancing the quality of water by preventing the direct discharge of waste effluents into water bodies. The increase in the absorption rate of waterbodies in this respect resulted in cooler temperatures (Jallu *et al*., 2022).

The effects of COVID-19-caused lockdowns on NDBI, NDVI, and LSTs in urban areas can be related to Sustainable Development Goal (SDG) 11 (Sustainable Cities and Communities). Large-scale changes to urban environments were caused by lockdowns, which were implemented to slow down the spread of the virus. In fact, lockdowns changed land use patterns

in that they reduced the scale of human activities. In certain places, owing to the lower levels of human-induced pollution and human interference, higher NDVI indices and a denser vegetational cover were the outcomes. This observation is supported by Li et al. (2020), who highlighted the fact that a reduction in human activities during the lockdown resulted in lower air pollutant emissions, which improved the quality of the air and led in turn to better land use patterns. In contrast, limitations and variations in human movement and shifts in the focus areas of economic activity caused variations in the NDBI index, which represents built-up areas. The repercussions of the landscape changes thus brought about served to promote the vision of a sustainable urban environment, a goal closely related to SDG 11. By comprehending these alterations, urban planners and policymakers can thus be supported in formulating tactics to increase urban resilience, refine urban planning, and foster sustainable development in urban regions, thereby contributing to the realisation of SDG 11.

Overall, the COVID-19 lockdown reduced LSTs in both Polokwane and Johannesburg. It is common knowledge that high LST values prevail in high density built-up areas, on bare land and on roads, while low LST values are associated with vegetated areas and waterbodies. Furthermore, the development of built-up and impervious surfaces, leading to changes in the urban environment in the form of LULC substantially impacts the temperature. This was found to be the case in the two cities. Through these processes, the transmission of energy and moisture between land and atmosphere altered in these two study areas, and the energy exchange resulted in temperature increases (Mushore *et al*., 2017).

This research proves that the actions implemented to manage the spread of COVID-19 improved the atmospheric conditions and biological and physical characteristics of the study areas. The findings of this study can better inform researchers, policymakers, decision-makers, town planners, and other stakeholders in urban planning as to the contributions that they could make in formulating future policies and implementing actions to enhance the sustainable development of cities.

5. Conclusion

This study used multitemporal Landsat satellite images to analyse LSTs in two South African cities, namely, Polokwane, and Johannesburg, before, during, and after the COVID-19 lockdowns in 2020, 2021, and 2022, respectively. The UHIs and UHSs in Polokwane and Johannesburg were investigated and compared over the entire study period (i.e., before, during, and after the COVID-19 lockdown). Linear regression models were employed at the pixel level to examine the dynamic associations between both the NDVI and NDBI and LSTs. This study found inverse correlations between NDVI and LST, and positive correlations between NDBI and LST. The lockdown, which was put in place in early March 2020, was a vital step taken by the government of South Africa to prevent the COVID-19 virus from spreading. The

monitoring of the satellite imagery indicated that this lockdown helped lower LSTs in the two study areas. For both cities, the highest LST values were for the built-up class before the COVID-19 lockdown in 2020; conversely, the lowest values were for the waterbody class during the lockdown in 2021. Overall, the COVID-19 lockdown had a notable impact on reducing the LSTs in Polokwane and Johannesburg. The decline in LSTs was due to the cessation of industrial activities, transportation, and other human activities, which all resulted in improved air quality that in turn mitigated the effects of the UHIs.

6. Future research

Future research will aim to retrieve LSTs using other methods and/or remote sensing data with different spatial resolutions. Furthermore, an attempt will be made at data fusion, which would depend on the compatibility of multi-source remote sensing and sophisticated data integration techniques. In addition to linear regression, novel statistical methods will be employed to assess the correlations between other LULC indices and LST. Finally, error matrices only estimate classification accuracy by applying samples acquired from the field. As such, biased conclusions can be made from such data. Therefore, other metrics of model performance, such as Matthew's Correlation Coefficient, the balanced accuracy method, and the F-sore bias score can be applied.

7. References

Adeyeri, O. E., Akinsanola, A. A., & Ishola, K. A. (2017). Investigating surface urban heat island characteristics over Abuja, Nigeria: Relationship between land surface temperature and multiple vegetation indices. *Remote Sensing Applications: Society and Environment, 7*, 57-68. https://doi.org/10.1016/j.rsase.2017.06.005

Alexander, C. (2020). Normalised difference spectral indices and urban land cover as indicators of land surface temperature (LST). *International Journal of Applied Earth Observation and Geoinformation, 86*. https://doi.org/10.1016/j.jag.2019.102013

Ali, G., Abbas, S., Qamer, F. M., Wong, M. S., Rasul, G., Irteza, S. M., & Shahzad, N. (2021). Environmental impacts of shifts in energy, emissions, and urban heat island during the COVID-19 lockdown across Pakistan. *Journal of Cleaner Production, 291*, 125806. https://doi.org/https://doi.org/10.1016/j.jclepro.2021.125806

Almeida, C. R. d., Teodoro, A. C., & Gonçalves, A. (2021). Study of the Urban Heat Island (UHI) using Remote Sensing Data/Techniques: A Systematic Review. *Environments, 8*(10). https://doi.org/10.3390/environments8100105

Alqasemi, A. S., Hereher, M. E., Kaplan, G., Al-Quraishi, A. M. F., & Saibi, H. (2021). Impact of COVID-19 lockdown upon the air quality and surface urban heat island intensity over the United Arab Emirates. *Science of the Total Environment, 767*, 144330.

Amani-Beni, M., Zhang, B., Xie, G.-D., & Shi, Y. (2019). Impacts of Urban Green Landscape Patterns on Land Surface Temperature: Evidence from the Adjacent Area of Olympic Forest Park of Beijing, China. *Sustainability, 11*(2). https://doi.org/10.3390/su11020513

Chakraborty, B., Bera, B., Adhikary, P. P., Bhattacharjee, S., Roy, S., Saha, S., Ghosh, A., Sengupta, D., & Shit, P. K. (2021). Positive effects of COVID-19 lockdown on river water quality: evidence from River Damodar, India. *Scientific Reports, 11*(1), 20140. https://doi.org/10.1038/s41598-021-99689-9

Chakraborty, T., Sarangi, C., & Lee, X. (2021). Reduction in human activity can enhance the urban heat island: Insights from the COVID-19 lockdown. *Environmental Research Letters, 16*(5), 054060.

Chavez, P. S. (1996). Image-based atmospheric corrections −revisited and improved. *Photogrammetric Engineering and Remote Sensing, 62*(9), 1025-1035.

Chen, X.-L., Zhao, H.-M., Li, P.-X., & Yin, Z.-Y. (2006). Remote sensing image-based analysis of the relationship between urban heat island and land use/cover changes. *Remote Sensing of Environment, 104*(2), 133-146.

Department of the Interior United States Geological Survey. (2019). *Landsat 8 (L8) Data Users Handbook*. Retrieved from: https://www.usgs.gov/media/files/landsat-8-data-users-handbook. (Date accessed: 30 April 2024.)

Emerson, R. W. (2015). Causation and Pearson's correlation coefficient. *Journal of Visual Impairment and Blindness, 109*(3), 242-244.

Errebai, F. B., Strebel, D., Carmeliet, J., & Derome, D. (2022). Impact of urban heat island on cooling energy demand for residential building in Montreal using meteorological simulations and weather station observations. *Energy and Buildings*, 112410.

Gillespie, A., Rokugawa, S., Matsunaga, T., Cothern, J. S., Hook, S., & Kahle, A. B. (1998). A temperature and emissivity separation algorithm for Advanced Spaceborne Thermal Emission and Reflection Radiometer (ASTER) images. *IEEE Transactions on Geoscience and Remote Sensing, 36*(4), 1113-1126.

Guha, S., Govil, H., Dey, A., & Gill, N. (2018). Analytical study of land surface temperature with NDVI and NDBI using Landsat 8 OLI and TIRS data in Florence and Naples city, Italy. *European Journal of Remote Sensing, 51*(1), 667-678.

Guha, S., Govil, H., & Mukherjee, S. (2017). Dynamic analysis and ecological evaluation of urban heat islands in Raipur city, India. *Journal of Applied Remote Sensing, 11*(3), 036020-036020.

Harlan, S. L., & Ruddell, D. M. (2011). Climate change and health in cities: impacts of heat and air pollution and potential co-benefits from mitigation and adaptation. *Current Opinion in Environmental Sustainability, 3*(3), 126-134. https://doi.org/https://doi.org/10.1016/j.cosust.2011.01.001

Hart, M. A., & Sailor, D. J. (2009). Quantifying the influence of land-use and surface characteristics on spatial variability in the urban heat island. *Theoretical and Applied Climatology, 95*(3), 397-406. https://doi.org/10.1007/s00704-008-0017-5

International Monetary Fund. (2023). *World Economic Outlook*. Retrieved from: https://www.imf.org/en/Publications/WEO?page=2. (Date accessed: 28 April 2024)

Irons, J. R., Dwyer, J. L., & Barsi, J. A. (2012). The next Landsat satellite: The Landsat data continuity mission. *Remote Sensing of Environment, 122*, 11-21.

Jackson, R., Slater, P., & Pinter Jr, P. (1983). Discrimination of growth and water stress in wheat by various vegetation indices through clear and turbid atmospheres. *Remote Sensing of Environment, 13*(3), 187-208.

Jallu, S. B., Shaik, R. U., Srivastav, R., & Pignatta, G. (2022). Assessing the effect of Covid-19 lockdown on surface urban heat island for different land use /cover types using remote sensing. *Energy Nexus, 5*, 100056. https://doi.org/10.1016/j.nexus.2022.100056

Jimenez-Munoz, J. C., Cristóbal, J., Sobrino, J. A., Sòria, G., Ninyerola, M., & Pons, X. (2008). Revision of the single-channel algorithm for land surface temperature retrieval from Landsat thermal-infrared data. *IEEE Transactions on Geoscience and Remote Sensing, 47*(1), 339-349.

Jiménez-Muñoz, J. C., & Sobrino, J. A. (2003). A generalized single-channel method for retrieving land surface temperature from remote sensing data. *Journal of Geophysical Research: Atmospheres, 108* (D22).

Jombo, S., Adam, E., Byrne, M. J., Ali, K. A., & Newete, S. W. (2020). Exploring the Potential of Feature Selection Methods in the Classification of Urban Trees using Field Spectroscopy Data. *International Journal of Geospatial and Environmental Research, 7*(3), 3.

Jombo, S., Adam, E., Byrne, M. J., & Newete, S. W. (2022). Assessing the intraurban differences in vegetation coverage and surface climate in a heterogeneous area. *Transactions of the Royal Society of South Africa*, 1-10. https://doi.org/10.1080/0035919x.2021.2004470

Khutso, M., Frank, R. S., & Justin, R. D. (2022). Sustainable Livelihoods for the International Female Migrant Youth in South Africa: The Case of Female Refugees in a Selected Church in Musina. *e-BANGI, 19*(1), 206-215. https://ezproxy.ufs.ac.za/scholarly-journals/sustainable-livelihoods-international-female/docview/2651852157/se-2?accountid=17207

Larsen, L. (2015). Urban climate and adaptation strategies. *Frontiers in Ecology and the Environment, 13*(9), 486-492.

Li, Y., Sun, Y., Li, J., & Gao, C. (2020). Socioeconomic drivers of urban heat island effect: Empirical evidence from major Chinese cities. *Sustainable Cities and Society, 63*, 102425. https://doi.org/https://doi.org/10.1016/j.scs.2020.102425

Liu, L., & Zhang, Y. (2011). Urban heat island analysis using the Landsat TM data and ASTER data: A case study in Hong Kong. *Remote Sensing, 3*(7), 1535-1552.

Logan, T. M., Zaitchik, B., Guikema, S., & Nisbet, A. (2020). Night and day: The influence and relative importance of urban characteristics on remotely sensed land surface temperature. *Remote Sensing of Environment, 247*, 111861. https://doi.org/10.1016/j.rse.2020.111861

Louw, A. S., Fu, J., Raut, A., Zulhilmi, A., Yao, S., McAlinn, M., Fujikawa, A., Siddique, M. T., Wang, X., Yu, X., Mandvikar, K., & Avtar, R. (2022). The role of remote sensing during a global disaster: COVID-19 pandemic as case study. *Remote Sensing Applications: Society and Environment, 27*, 100789. https://doi.org/https://doi.org/10.1016/j.rsase.2022.100789

Lu, Q., Liang, F., Bi, X., Duffy, R., & Zhao, Z. (2011). Effects of urbanization and industrialization on agricultural land use in Shandong Peninsula of China. *Ecological Indicators, 11*(6), 1710-1714.

Ma, Y., Kuang, Y., & Huang, N. (2010). Coupling urbanization analyses for studying urban thermal environment and its interplay with biophysical parameters based on TM/ETM+ imagery. *International Journal of Applied Earth Observation and Geoinformation, 12*(2), 110-118.

Magli, S., Lodi, C., Lombroso, L., Muscio, A., & Teggi, S. (2015). Analysis of the urban heat island effects on building energy consumption. *International Journal of Energy and Environmental Engineering, 6*(1), 91-99. https://doi.org/10.1007/s40095-014-0154-9

Maithani, S., Nautiyal, G., & Sharma, A. (2020). Investigating the Effect of Lockdown during COVID-19 on Land Surface Temperature: Study of Dehradun City, India. *Journal of the Indian Society of Remote Sensing, 48*(9), 1297-1311. https://doi.org/10.1007/s12524-020-01157-w

Masek, J. G., Wulder, M. A., Markham, B., Mccorkel, J., Crawford, C. J., Storey, J., & Jenstrom, D. T. (2020). Landsat 9: Empowering open science and applications through continuity. *Remote Sensing of Environment, 248*, 111968. https://doi.org/10.1016/j.rse.2020.111968

Mathew, A., Khandelwal, S., & Kaul, N. (2016). Spatial and temporal variations of urban heat island effect and the effect of percentage impervious surface area and elevation on land surface temperature: Study of Chandigarh city, India. *Sustainable Cities and Society, 26*, 264-277.

Mishra, K., & Garg, R. D. (2023). Assessing variations in land cover-land use and surface temperature dynamics for Dehradun, India, using multi-time and multi-sensor Landsat data. *Environmental Monitoring and Assessment, 195*(3), 373. https://doi.org/10.1007/s10661-023-10945-z

Montanaro, M., Gerace, A., Lunsford, A., & Reuter, D. (2014). Stray light artifacts in imagery from the Landsat 8 Thermal Infrared Sensor. *Remote Sensing, 6*(11), 10435-10456.

Mudede, M. F., Newete, S. W., Abutaleb, K., & Nkongolo, N. (2020). Monitoring the urban environment quality in the city of Johannesburg using remote sensing data. *Journal of African Earth Sciences, 171*. https://doi.org/10.1016/j.jafrearsci.2020.103969

Mushore, T. D., Mutanga, O., Odindi, J., & Dube, T. (2017). Linking major shifts in land surface temperatures to long-term land use and land cover changes: A case of Harare, Zimbabwe. *Urban Climate, 20*, 120-134. https://doi.org/10.1016/j.uclim.2017.04.005

Mustafa, E. K., Co, Y., Liu, G., Kaloop, M. R., Beshr, A. A., Zarzoura, F., & Sadek, M. (2020). Study for Predicting Land Surface Temperature (LST) using Landsat Data: A Comparison of Four Algorithms. *Advances in Civil Engineering, 2020*, 1-16. https://doi.org/10.1155/2020/7363546

NASA. (2022). *Landsat Science*. Retrieved from: https://landsat.gsfc.nasa.gov/satellites/landsat-9/landsat-9-instruments/. (Date accessed: 13 May 2024)

Njoku, P. O., & Edokpayi, J. N. (2022). Estimation of landfill gas production and potential utilisation in a South Africa landfill. *Journal of the Air and Waste Management Association* (just-accepted).

Onishi, A., Cao, X., Ito, T., Shi, F., & Imura, H. (2010). Evaluating the potential for urban heat-island mitigation by greening parking lots. *Urban Forestry and Urban Greening, 9*(4), 323-332.

Patra, S., Sahoo, S., Mishra, P., & Mahapatra, S. C. (2018). Impacts of urbanization on land use /cover changes and its probable implications on local climate and groundwater level. *Journal of Urban Management, 7*(2), 70-84. https://doi.org/10.1016/j.jum.2018.04.006

Pörtner, H.-O., Roberts, D. C., Adams, H., Adler, C., Aldunce, P., Ali, E., Begum, R. A., Betts, R., Kerr, R. B., & Biesbroek, R. (2022). Climate change 2022: Impacts, adaptation and vulnerability. *IPCC Sixth Assessment Report*.

Purevdorj, T., Tateishi, R., Ishiyama, T., & Honda, Y. (1998). Relationships between percent vegetation cover and vegetation indices. *International Journal of Remote Sensing, 19*(18), 3519-3535.

Qin, Z., Karnieli, A., & Berliner, P. (2001). A mono-window algorithm for retrieving land surface temperature from Landsat TM data and its application to the Israel-Egypt border region. *International Journal of Remote Sensing, 22*(18), 3719-3746. https://doi.org/10.1080/01431160010006971

Rachuene, P., Masipa, R., Dey, R., Msingapantsi, M., Khanyile, S., Phala, M., Murila, J., & Mariba, M. (2021). The impact of COVID-19 national lockdown on orthopaedic trauma admissions in the northern part of South Africa: A multicentre review of tertiary and secondary-level hospital admissions. *South African Medical Journal, 111*(7), 668-673.

Rajeshwari, A., & Mani, N. (2014). Estimation of land surface temperature of Dindigul district using Landsat 8 data. *International Journal of Research in Engineering and Technology, 3*(5), 122-126.

Rogerson, C. M., & Rogerson, J. M. (2021). Looking to the Past: The Geography of Tourism in South Africa during the Pre-COVID-19 Era. In C. M. Rogerson & J. M. Rogerson (Eds.), *Urban Tourism in the Global South: South African Perspectives,* 39-75. Springer International Publishing. https://doi.org/10.1007/978-3-030-71547-2_2

Shikwambana, L., Kganyago, M., & Mhangara, P. (2021). Temporal Analysis of Changes in Anthropogenic Emissions and Urban Heat Islands during COVID-19 Restrictions in Gauteng Province, South Africa. *Aerosol and Air Quality Research, 21*(9), 200437. https://doi.org/10.4209/aaqr.200437

Shochat, E., Warren, P. S., Faeth, S. H., McIntyre, N. E., & Hope, D. (2006). From patterns to emerging processes in mechanistic urban ecology. *Trends in Ecology and Evolution, 21*(4), 186-191. https://doi.org/https://doi.org/10.1016/j.tree.2005.11.019

Sobrino, J., Li, Z., Stoll, M., & Becker, F. (1996). Multi-channel and multi-angle algorithms for estimating sea and land surface temperature with ATSR data. *International Journal of Remote Sensing, 17*(11), 2089-2114.

Sobrino, J., Raissouni, N., & Li, Z.-L. (2001). A comparative study of land surface emissivity retrieval from NOAA data. *Remote Sensing of Environment, 75*(2), 256-266.

Sobrino, J. A., Jiménez-Muñoz, J. C., & Paolini, L. (2004). Land surface temperature retrieval from Landsat TM 5. *Remote Sensing of Environment, 90*(4), 434-440.

Solanky, V., Singh, S., & Katiyar, S. K. (2018). Land Surface Temperature Estimation using Remote Sensing Data. *Hydrologic Modeling*, Singapore.

South African Government. (2023). *COVID-19 / Coronavirus*. Retrieved from: https://www.gov.za/Coronavirus. (Date accessed: 28 April 2024)

South African Weather Service. (2022). *Polokwane*. Retrieved from: https://www.weathersa.co.za/. (Date accessed: 04 September 2024)

Stathopoulou, M., & Cartalis, C. (2007). Daytime urban heat islands from Landsat ETM+ and Corine land cover data: An application to major cities in Greece. *Solar Energy, 81*(3), 358-368.

Statistics South Africa. (2022). *Statistical Publications*. Retrieved from: http://www.statssa.gov.za/?page_id=964. (Date accessed: 03 January 2024)

Su, F., Fu, D., Yan, F., Xiao, H., Pan, T., Xiao, Y., Kang, L., Zhou, C., Meadows, M., Lyne, V., Wilson, J. P., Zhao, N., Yang, X., & Liu, G. (2021). Rapid greening response of China's 2020 spring vegetation to COVID-19 restrictions: Implications for climate change. *Science Advances, 7*(35), eabe8044. https://doi.org/doi:10.1126/sciadv.abe8044

Tarawally, M., Xu, W., Hou, W., & Mushore, T. (2018). Comparative Analysis of Responses of Land Surface Temperature to Long-term Land Use/Cover Changes between a Coastal and Inland City: A Case of Freetown and Bo Town in Sierra Leone. *Remote Sensing, 10*(1). https://doi.org/10.3390/rs10010112

Tleane, S. J., & Ndambuki, J. M. (2020). Estimation of Groundwater Recharge using GIS Method: A Case Study of Makotopong Village — Polokwane, South Africa. *Journal of Water Resource and Protection, 12*(11), 985-1000. https://doi.org/10.4236/jwarp.2020.1211059

Tucker, C. J. (1979). Red and photographic infrared linear combinations for monitoring vegetation. *Remote Sensing of Environment, 8*(2), 127-150. https://doi.org/https://doi.org/10.1016/0034-4257(79)90013-0

United Nations. (2022). *UN issues new guidance to address warming in cities*. United Nations. Retrieved from: https://www.unep.org/news-and-stories/press-release/un-issues-new-guidance-address-warming-cities. (Date accessed: 24 August 2024)

United States Environmental Protection Agency. (2008). *Reducing Urban Heat Islands: Compendium of Strategies*. Retrieved from: https://www.epa.gov/heat-islands/heat-island-compendium. (Date accessed: 28 April 2024)

University Corporation for Atmospheric Research. (2011). *Urban Heat Islands*. Retrieved from: https://scied.ucar.edu/longcontent/urban-heat-islands. (Date accessed: 28 April 2024)

Wang, Y., Berardi, U., & Akbari, H. (2016). Comparing the effects of urban heat island mitigation strategies for Toronto, Canada. *Energy and Buildings, 114*, 2-19. https://doi.org/https://doi.org/10.1016/j.enbuild.2015.06.046

Weng, Q., Lu, D., & Schubring, J. (2004). Estimation of land surface temperature–vegetation abundance relationship for urban heat island studies. *Remote Sensing of Environment, 89*(4), 467-483.

Wiedermann, W., & Hagmann, M. (2016). Asymmetric properties of the Pearson correlation coefficient: Correlation as the negative association between linear regression residuals. *Communications in Statistics - Theory and Methods, 45*(21), 6263-6283. https://doi.org/10.1080/03610926.2014.960582

World Health Organisation. (2023). *WHO Coronavirus (COVID-19) Dashboard*. Retrieved from: https://covid19.who.int/. (Date accessed: 28 April 2024)

World Population Review. (2022). *World Population Review*. Retrieved from: https://worldpopulationreview.com/world-cities/polokwane-population. (Date accessed: 04 September 2024)

Zambrano-Monserrate, M. A., Ruano, M. A., & Sanchez-Alcalde, L. (2020). Indirect effects of COVID-19 on the environment. *Science of the Total Environment, 728*, 138813.

Zha, Y., Gao, J., & Ni, S. (2003). Use of normalized difference built-up index in automatically mapping urban areas from TM imagery. *International Journal of Remote Sensing, 24*(3), 583-594.

Zhao, H., & Chen, X. (2005). Use of normalized difference bareness index in quickly mapping bare areas from TM/ETM+. In International Geoscience and Remote Sensing Symposium (Vol. 3, p. 1666).